Versatile functionality of four-terminal TiO_{2-x} memristive devices as artificial synapses for neuromorphic computing

Ryotaro Miyake[1], Zenya Nagata[1], Kenta Adachi[1], Yusuke Hayashi[1], Tetsuya Tohei[1*], and Akira Sakai[1*]

[1] Graduate School of Engineering Science, Osaka University, 1-3 Machikaneyama-cho, Toyonaka, Osaka 560-8531, Japan

[*]E-mail: tohei@ee.es.osaka-u.ac.jp; sakai@ee.es.osaka-u.ac.jp

Keywords: artificial synapse, memristive device, hetero-synaptic, neuromodulation, reduced TiO_{2-x}, gate-tuning, multi-terminal, resistive switching.

Abstract

Brain-inspired computing systems, which emulate the activity of biological synapses and neurons, are becoming more and more essential owing to their potential ability to solve the von Neumann bottleneck. Various types of memristive devices have been proposed to achieve information processing through synaptic functions. However, biological synapses have many complicated functions, such as hetero-synaptic plasticity and the related neuromodulation, that are difficult to implement in conventional two-terminal memristors because of the requirement for multiple inputs. In this study, simple four-terminal memristive devices consisting of epitaxial thin films of TiO_{2-x} are fabricated and their capacity to implement synaptic functions are explored. These devices utilize the two-dimensional variation of the oxygen vacancy distribution in the TiO_{2-x} film to realize advanced hetero-synaptic functionality, including tunable spike-timing-dependent plasticity, hetero-synaptic plasticity mimicking habituation and sensitization, and Pavlovian conditioning, through multi-terminal voltage inputs. The present results demonstrate the striking versatility of our four-terminal device for implementing the diverse and complex functions of artificial synapses on a single memristive passive element.

1. Introduction

Recent advances in artificial intelligence technology have attracted great attention. At the same time, they have highlighted a problem associated with present technologies known as the bottleneck of von-Neumann-architecture computers. One solution to this problem is to employ new computing architectures inspired by a biological brain. Neural systems in the brain and related biological cellular components are effective in handling complicated tasks with the action of synapses.[1-4] Consequently, artificial synapses, used to mimic the function of such bio-synapses, are crucial building blocks for constructing a hardware-based neural network in high-efficiency brain-inspired computing systems. Memristive devices have often been used as artificial synapses to closely emulate several neuromorphic properties,[5-13] in which resistive switching, equivalent to the alteration of synaptic weight in neural systems, occurs in a non-volatile manner by applying external voltages to the devices.[14,15] Reduced TiO_2 (TiO_{2-x}) is one promising candidate memristive material,[16-18] its inherent oxygen vacancies acting as ionic donors contributing to resistive switching.

Recently, we have developed memristive devices with a unique four-terminal configuration using TiO_{2-x} single-crystal substrates.[19-21] The four-terminal configuration is unique in that the resistance is determined by the two-dimensional distribution of oxygen vacancies in the electrically active zone, which can be controlled precisely by external voltages applied to the four terminal electrodes. Since oxygen vacancies have a positive charge, their distribution can be modulated through drift motion caused by the electric field in the device. This working principle widens the possibilities of mimicking higher-order brain and neuromorphic functions. The biological synapse has an intriguing function called hetero-synaptic plasticity, *i.e.*, modulatable plasticity induced by multiple connections of synapses and specific cellular mechanisms.[22-25] This heterogeneity gives rise to learning functions such as associative learning and other types of behavioral learning.[1,26,27] Although conventional two-terminal memristors have been employed so far for imparting hetero-synaptic properties in a number of complex manners,[10,28-32] the multi-terminal configuration is essential for improving the versatility of hetero-synaptic functions.[20,21,33-49]

In this study, we use conductive TiO_{2-x} epitaxial thin films grown on insulating TiO_2 substrates as a memristive material. The superiority of these epitaxial thin films, employed

in place of the previously used thermally-reduced substrates,[20,21] is demonstrated on the basis of several memristive properties. Four-terminal devices are fabricated, consisting of two pairs of electrodes arranged diagonally, each pair having a different role: one pair is used as a homo-synapse for read/write operations, while the other pair is for gating operations corresponding to the action of the hetero-synapse and neuromodulator. The application of a gate voltage induces a two-dimensional modulation of the oxygen vacancy distribution, producing a rich variety of resistive switching properties and thus enabling higher-order neuromorphic functionality as the artificial hetero-synapse. Here we demonstrate the implementation of versatile behavior, such as spike-timing-dependent plasticity (STDP), habituation and sensitization, and Pavlovian conditioning known as associative learning, all of which become tunable with the help of heterogeneity functioning in a single memristive device.

2. Results and Discussion

2.1. Oxygen vacancy distribution and resistive switching

An optical micrograph of the four-terminal planar device formed with a TiO_{2-x} epitaxial thin film is shown in **Figure 1**a. We utilized (001) plane of rutile TiO_2 since this crystal orientation allows reversible change of two-dimensional oxygen vacancy distribution on applied voltages.[20,21] The device has two pairs of diagonally opposed square Pt electrodes. To firstly examine the resistive switching performance of the device, electrical measurements were performed by applying voltages according to the sequence shown in **Figure 1**b. The conductance value $G_{1\text{-}3}$ ($G_{2\text{-}4}$) between terminals T1 (T2) and T3 (T4), was measured while applying a voltage V_1 (V_2) to T1 (T2) as a read voltage while T3 (T4) was grounded. Subsequently, write voltages $V_{2,4}$ were simultaneously applied to both T2 and T4 for a certain period t while T1 and T3 were grounded. This cycle was repeated while ramping the voltage $V_{2,4}$ up and down over the range between the maximum voltage V_M and the minimum voltage V_m in 1 V steps. Since oxygen vacancies have a positive charge, it is expected that applying positive (negative) voltage to terminals T2 and T4 (i.e. $V_{2,4}$) concentrate oxygen vacancies around terminals T1 and T3 (T2 and T4), and make a bridge of conductive regions between T1 and T3 (T2 and T4), as will be shown later. This would

bring high $G_{1\text{-}3}$ ($G_{2\text{-}4}$) and low $G_{2\text{-}4}$ ($G_{1\text{-}3}$), and the conductance states should be inverted according to the changing $V_{2,4}$ voltage polarity.

Figure 2a (2b) shows variations of $G_{1\text{-}3}$ ($G_{2\text{-}4}$) as a function of applied $V_{2,4}$, measured for the device having a $TiO_{2\text{-}x}$ film with a thickness of 65 nm and a resistivity of 2.8×10^{-3} Ω· cm with V_M = +8 V and V_m = -8 V for t = 100 s, where the cycle was repeated six times. When $G_{1\text{-}3}$ increases, $G_{2\text{-}4}$ decreases, and vice versa, indicating that the $G_{1\text{-}3}$ and $G_{2\text{-}4}$ variations are complementary. This is a unique characteristic of our four-terminal device. With increasing $V_{2,4}$, a sharp increase (decrease) in $G_{1\text{-}3}$ ($G_{2\text{-}4}$), a so-called SET (RESET) operation, occurs at +6 V, so that a high conductance state HCS (low conductance state LCS) is achieved. After the SET (RESET) operation occurs, with decreasing $V_{2,4}$, a sharp decrease (increase) in $G_{1\text{-}3}$ ($G_{2\text{-}4}$) occurs at -6 V, so that a LCS (HCS) is achieved. In more detail, we observed that from HCS to LCS of $G_{1\text{-}3}$ and $G_{2\text{-}4}$ shows a region of gradual change, but not in the transition from LCS to HCS. This may be because on approaching HCS states, local oxygen concentration is at high level at which the conductivity change becomes more insensitive to concentration change, bringing abrupt resistive change near the saturation voltage. Whereas on approaching LCS states, oxygen concentration is at low level where conductivity change becomes more sensitive to concentration change, this would bring gradual change in resistivity near the saturation region. By applying the voltages cyclically, the conductance can be tuned repeatedly. The maximum HCS-to-LCS conductance ratio was found to be more than 20 in the present thin-film based device. This is a remarkable improvement over our previous devices, in which we used thermally reduced rutile-TiO_2(001) single-crystal substrates and whose resistance ratio was 2 to 3.[20] Our obtained on/off ratio of 20 may be somewhat smaller than typically reported values for filamentary based memristors in which switching process is sharper but stochastic. Our device is based on bulk conducting mechanism rather than filamentary mechanism, aiming for improvement of yield and stability and resulting in moderate on/off ratio. Although further improvement of on/off ratio is desirable, tuning of multi-valued conductance states (synaptic weight) is possible in enough resolution as demonstrated in our previous report[21] and results shown in later sections.

We also performed microscopic observations of the device to elucidate the resistive switching mechanism during the cyclic application of $V_{2,4}$. The variation in the oxygen

vacancy distribution, which accounts for the change in the conductance state of TiO_{2-x}, can be visualized by exploiting the electro-coloring phenomenon.[50,51] The local concentration of oxygen vacancies is well reflected in the color of the TiO_{2-x} crystal; a region with a higher (lower) concentration of oxygen vacancies appears bluish (colorless)[20]. Our previous electron energy loss spectroscopy studies have demonstrated that reduced Ti valence states in the colored region are responsible for the occurrence of the HCS.[19,21] **Figures 2**c and 2d show optical micrographs of the device at the stages of $V_{2,4}$ = +8 V and -8 V in the second cycle, respectively. The observed colored (colorless) region around T1 and T3 shown in **Figure 2**c (2d) indicates accumulation (depletion) of oxygen vacancies due to positive (negative) $V_{2,4}$ application, well reflecting the measured conductance increase (decrease) between T1 and T3. Thus, we can establish a direct correlation between the two-dimensional redistribution of oxygen vacancies and the resistive switching properties.

2.2. Numerical simulation of two-dimensional oxygen vacancies and electron conduction

Several numerical modeling approaches have been followed to date to gain a physical understanding of resistive switching. In principle, a model based on numerical solutions of coupled drift-diffusion equations for electrons and ions in a doped semiconductor thin film provides physical insights into the dynamics of electronic and ionic transport processes.[52-54] For our four-terminal devices, to verify the two-dimensional redistribution behavior of oxygen vacancies, *i.e., n*-type dopants, through the drift and diffusion model, we performed numerical simulations based on the finite element method. **Figures 3**a and 3b show simulation results for the dopant distribution modified by applying a voltage with the same waveform as that in **Figure 1**b. After applying V_M (V_m), the dopants accumulate at the peripheries of T1 (T2) and T3 (T4) and are distributed around them, shown in light green color. These simulation results well reproduce the observed features of the colored regions in **Figures 2**c and 2d.

Figures 3c and 3d depict the simulated current density distributions subjected to an applied read voltage V_{read} for the dopant distributions shown in **Figures 3**a and 3b, respectively. When dopants accumulate between T1 and T3, higher current density areas

bridge T1 and T3, whereas no such areas are formed in the case of accumulation between T2 and T4, which is also consistent with the experimentally measured conductance states, as shown in **Figures 2**a and 2b. This agreement between the simulated and experimentally observed behavior validates our proposed model based on two-dimensional oxygen vacancy redistribution as a mechanism for the resistive switching phenomena occurring in the four-terminal device.

2.3. Tunable spike-timing-dependent plasticity

Next, we tried to impart synaptic functions to the four-terminal memristive device. In this study, we applied voltage pulses V_1 to T1, with T3 grounded, to modulate the conductance $G_{1\text{-}3}$. This voltage application protocol emulates the synaptic plasticity between pre- and post-synapse. In addition, gate voltage pulses V_{gate} were applied to both T2 and T4, being synchronized to V_1 to mimic the signal transmission from interneurons or a neuromodulator, as illustrated in **Figure 4**.

STDP is a Hebbian synaptic learning rule that is often demonstrated in biological experiments.[55,56] The synaptic weight reflecting the strength of the connection between neurons is modulated by pre- and post-synaptic activities and depends on the relative timing of the pre- and post-synaptic spikes. In other words, the synaptic weight change Δw is a function of Δt, where Δt represents the time difference between two spikes. In canonical asymmetric Hebbian STDP, when the pre-spike precedes the post-spike ($\Delta t > 0$), the connection of synapses is strengthened, while when the post-spike precedes the pre-spike ($\Delta t < 0$), the connection is weakened. Other kinds of Hebbian STDP have been confirmed in biological systems as well, such as asymmetric anti-Hebbian and symmetric Hebbian rules.[57-61]

Implementation of STDP as the functionality of artificial synapses has been demonstrated in various types of memristive devices,[62-66] where two-terminal devices are commonly utilized for inputting the pre- and post-spikes to change the device conductance as a synaptic weight. However, synaptic weight modulation in STDP has so far been rarely demonstrated in a hetero-synapse configuration. Here, we attempted to implement STDP in our four-terminal devices and perform gate modulation of STDP characteristics. To reproduce this behavior, we have to utilize pre-/gate- and post- spikes that have both

positive and negative components in the waveform. Arbitrary wave forms that meet the condition can be used as pre-/gate- and post- spike. In this study we used spikes that are formed by simple combination of positive and negative square pulses. The designed spike pulse schemes for pre- and post-spikes and a gate spike are shown in **Figures 5**a and 5b, respectively. The spike composed of positive and negative voltage pulses (V_1 = ±7 V, 25 ms) was used for the pre/post-spikes and applied to the device with a time difference Δt. The gate spike pulse with a voltage amplitude V_{gate} as a variable (the upper part of **Figure 5**b) was applied for the gate modulation, while the pulse width and the timing were the same as those for the pre-spike. The total effective voltage pulses on the device are shown in the lower parts of **Figures 5**a and 5b, and in practice, these pulse schemes were applied to T1 for the input of the pre/post-spikes and to both T2 and T4 for the gate modulation while T3 was grounded. **Figure 5**c shows the detailed voltage application protocol. First, a read voltage of 100 mV was applied to T1 to measure the conductance between T1 and T3, then 12 V was applied to the gate terminals (T2 and T4) for 50 s to concentrate oxygen vacancies between T1 and T3, and voltage pulses were then applied to T1 to initialize the device conductance to a certain value. Next, as the first STDP process, the V_1 spike was applied to T1 and the device conductance was measured before and after the application. After initialization, as the second STDP process, the V_{gate} spike was applied to T2 and T4 simultaneously with V_1 application. This measurement cycle was repeated with changing Δt.

Figures 5d to 5k show the observed variations of synaptic weight Δw as a function of Δt, where

$$\Delta w = \frac{G_{\text{after}} - G_{\text{before}}}{G_{\text{before}}} \times 100\ [\%]. \qquad (1)$$

Figure 5d shows the result for the case where no gate spike was applied, in which canonical asymmetric Hebbian STDP is clearly reproduced, featuring the occurrence of potentiation (positive Δw) when $\Delta t > 0$ and depression (negative Δw) when $\Delta t < 0$. The probable physical cause of the observed response behavior is that, when Δt is positive, effective negative voltage pulses are applied to T1 so that the oxygen-vacancy-accumulated region extends over the T1 side, leading to a conductance increase. On the other hand, when Δt is negative, the effective positive voltage pulses

applied to T1 could repel oxygen vacancies, resulting in a conductance decrease. We note that the STDP characteristics can be modulated systematically by simultaneous application of the gate spike. With increasing V_{gate}, $|\Delta w|$ decreases irrespective of the polarity of Δt, and further increasing V_{gate} to 7 V (**Figure 5**k) results in asymmetric anti-Hebbian STDP in which the synaptic weight change occurs in an inverse relationship to spike timing compared to canonical Hebbian STDP: post-leading-pre spike and pre-leading-post spike pairings lead to potentiation and depression, respectively. Since the V_{gate} spike scheme is determined by the employed values of V_{gate} and Δt as shown in **Figure 5**b, the V_{gate} increase causes an increase in the effective negative (positive) voltage pulse relative to the positive (negative) pulse for a positive (negative) Δt. Such an effective negative (positive) voltage pulse could induce enhanced dispersion (accumulation) of oxygen vacancies in the region between T1 and T3 and thus decrease (increase) the device conductance (Figure S5). In this way, the gate spike systematically tunes the amount of synaptic weight induced by STDP and controls the STDP rule in the forms of canonical Hebbian and anti-Hebbian as well as in the form of transient states.

It is noteworthy that the above gating operation plays a role in mimicking the neuromodulatory control of STDP, which often occurs in biological synapses. Indeed, STDP is not only controlled by temporal states during the spiking activity of pre- and postsynaptic neurons, but also by neuromodulation. Recent neurophysiology results have revealed that several neuromodulators, such as dopamine, noradrenaline, and monoamine, have a distinct influence on changing the polarity, shape and timing windows of STDP[67-75] and provide mechanisms for adjusting the synaptic weight to regulate the plasticity of synapses.[76] In biological nervous systems, implementation of not only canonical Hebbian but also anti-Hebbian STDP may prove advantageous for effective association and reinforcement learning[77-81], which could also enhance the computational power of neural networks composed of artificial synapses. In addition, it should be noted that the transient states of conversion from canonical Hebbian to anti-Hebbian, as seen at a V_{gate} of 5V in **Figure 5**i, can be regarded as silent synapses in which neurotransmission does not produce a response in the receiving cell. The maturation of silent synapses via unsilencing and stabilization is known to be a fundamental step in the development and refinement of neural networks in the brain.[82-87] On the other hand, in terms of machine learning using

deep neural networks, the formation of silent synapses corresponds to “dropout,” which is one effective technique used for regularization of neural network models: the nodes are “dropped” along with the connections from the neural network during training to prevent the model from overfitting.[88] As shown in Ref. 88, compared to other techniques such as solely introducing L1 and L2 regularization and model combination, dropout considerably improves the performance of standard neural networks on various types of data sets. In software based systems, one of the drawbacks of dropout is that it increases training time. Although this might also be the case in the hardware systems, our device enables modulation of STDP behaviors by gate operation and this allows arbitrary control of dynamic on/off state of artificial synapses as silent synapses. Such utilization is not achieved by other synaptic device hardware proposed so far. Thus, the configuration employed for the four terminals and the conductance control based on the oxygen vacancy distribution are demonstrated to have diverse functionalities as building blocks of neuromorphic computing systems.

2.4. Habituation and sensitization: heterogeneous control of synaptic plasticity

Extensive pioneering studies on habituation and sensitization have been conducted in biological systems, in particular, for the siphon- and gill-withdrawal reflex in the marine mollusc Aplysia. In the specific interneuronal circuit, which has been precisely identified, sensory neurons innervating the siphon are directly connected to motor neurons and indirectly connected through several excitatory and inhibitory interneurons.[89-92] Habituation occurs, with repeating presentation of a stimulus, in the form of a gradual decrease in the response to stimulus when the Aplysia learns that the stimulus is harmless. This learning results from a decrease in the strength of synaptic connections between sensory and motor neurons.[93,94] On the other hand, in sensitization, a general increase in response to neutral stimuli occurs, for example, after presentation of a noxious stimulus in the tail of Aplysia.[95,96] This behavioral response is caused by an increase in the strength of heterogeneous synapses in the set of connections between sensory and motor neurons.[1,94]

Here, we report the imparting of habituation and sensitization properties to a four-terminal device by the voltage application protocol illustrated in **Figures 6**a and 6b, respectively. In this experiment, voltage pulses V_1 are applied to T1, mimicking neutral

inputs from the sensory neuron of the siphon, while T3 is grounded. Positive and negative V_1 applications correspond to potentiation and depression (P/D) operations, respectively. The behavioral response of the motor neuron of the gill is characterized by the conductance $G_{1\text{-}3}$ between T1 and T3. As shown in **Figure 6**a, to implement the property of habituation, pulses of negative gate voltage V_{HG} are applied to both T2 and T4, as mimicking inputs from inhibitory interneurons, simultaneously with every potentiation operation in the P/D cycles. In the case of the sensitization shown in **Figure 6**b, the stimulation process is conducted prior to the P/D operation, in which pulses of positive gate voltage V_{SG} are applied to both T2 and T4 under a negative constant voltage application to T1, as mimicking inputs from interneurons connected to the tail being presented with a noxious stimulus. Note that V_{HG} is applied only in the stimulation process and not in the P/D processes.

Figure 6c shows the variation in $G_{1\text{-}3}$, normalized by the first maximum of the potentiated conductance, in 20 cycles of P/D operation under several conditions of V_{HG} application, in which consecutive 100-ms-wide pulses of V_1 with +10 and -10 V are applied for potentiation and depression, respectively. In the case where V_{HG} is not applied (n/a), a stable P/D waveform is observed. On the other hand, when V_{HG} is applied, the conductance increase becomes smaller in potentiation, and the conductance decreases more in depression, compared to the n/a case. The amplitude of the P/D waveform gradually decreases with increasing number of cycles, mimicking habituation, in which the response is decreased due to repeated stimuli. As an indicator, the degree of habituation is estimated using the amplitude of the conductance change in the first potentiation and that in the last potentiation, and the results are shown in **Figure 6**d. The degree of habituation clearly depends on the gate voltage: it increases with negatively increasing V_{HG}, indicating the feasibility of gate tuning for the habituation property.

Representative results for sensitization are shown in **Figure 6**e. Variations of $G_{1\text{-}3}$ were measured at non-applied gate voltage (n/a) and different V_{SG} in the range from 2 to 10 V; 100-ms-wide stimulation and P/D pulses were applied, respectively, 5 and 10/10 times after setting the initial $G_{1\text{-}3}$ to LCS (~1.6 mS). In the n/a and relatively low V_{SG} cases, there was little change in $G_{1\text{-}3}$. As V_{SG} increased to 6 V, $G_{1\text{-}3}$ was observed to increase slightly in both the stimulation and P/D processes. A further increase in V_{SG} initially led to a sharp increase in the stimulation process, which eventually dropped to a level comparable to the

6 V case. However, in the subsequent potentiation process, $G_{1\text{-}3}$ increased sharply and significantly. **Figure 6**f summarizes the $G_{1\text{-}3}$ values after initialization, stimulation, and application of 10 potentiation pulses as a function of V_{SG}. Note that $G_{1\text{-}3}$ increases sharply with increasing V_{SG}, mimicking sensitization: the stronger the stimulation, the higher the response.

On the basis of the oxygen vacancy distribution in the active zone of the four-terminal device, we infer the mechanisms behind the implemented habituation and sensitization behavior of the device. The application of a negative (positive) gate voltage induces a distribution of oxygen vacancies that is diluted (condensed) compared to the n/a case, in the region between T1 and T3 where the conductance change occurs. The diluted (condensed) oxygen vacancy distribution gives rise to a smaller (larger) conductance change per P/D pulse in habituation (sensitization), since the rate of conductance change depends on the concentration of oxygen vacancies as a dopant.[21] Therefore, with increasing absolute value of gate voltage, a larger modulation of the oxygen vacancy distribution is achieved, resulting in a smaller conductance variation in habituation and a larger attainable conductance in sensitization.

2.5. Pavlovian conditioning

A typical example of associative learning was described by Ivan Pavlov,[97] known as Pavlovian conditioning. In this case, a dog is observed to salivate whenever it senses the presence of food. Then, in a conditioning process, a bell is rung every time the dog is fed. As a result of the conditioning, the dog starts to salivate on hearing the bell even when no food is given. Thus, by feeding the dog and ringing the bell with temporal contiguity, the dog learns to associate the bell sound (neutral stimulus) with food (unconditioned stimulus). The behavior of Pavlov's dog is summarized in the truth table shown in **Table 1**.

Here, we performed a series of electrical measurements to implement Pavlovian learning to the four-terminal memristive device. As shown in **Figure 7**a, applications of voltages to T1 and T4 (V_1 and V_4, respectively) were assigned to the bell sound and food, respectively, and the resultant conductance $G_{1\text{-}3}$ between T1 and T3 was assumed to represent the response of a dog. We first conducted an initialization process, where a set of write voltages were applied to both T3 and T4 with both T1 and T2 grounded, to adjust

$G_{1\text{-}3}$ to a certain value of LCS and the conductance $G_{4\text{-}3}$ between T4 and T3 to a certain value of HCS. A high $G_{4\text{-}3}$ corresponded to the dog's natural reaction to food, i.e., the unconditioned stimulus. Then, voltage pulses of V_1 were applied repeatedly to simulate the bell sound. At every tenth application of V_1, a voltage pulse V_4 was applied simultaneously with the food. $G_{1\text{-}3}$ was measured after each application of V_1 by applying a non-disturbed voltage to T1, with T3 grounded.

Figure 7a shows an application sequence at a V_1 of -9 V and a V_4 of 9 V as well as the resultant conductance values of $G_{1\text{-}3}$. In the first series of V_1 pulse application before V_4 application, $G_{1\text{-}3}$ showed no significant change from its initial value of ~0.6 mS. After the simultaneous application of V_1 and V_4, a slight increase was observed in $G_{1\text{-}3}$. Then, the third simultaneous application of V_1 and V_4 at a pulse number of 30 caused $G_{1\text{-}3}$ to be increased sharply, which maintained high values afterwards only with the application of V_1. This result points to the phenomenon of conditioning: the dog associates the bell sound with food and learns to react to the bell sound alone. We also verified the phenomenon of forced forgetting, where $G_{1\text{-}3}$ could be reset to its initial value (~0.6 mS) by the initialization process at a pulse number of 40 and then no increase in $G_{1\text{-}3}$ occurred with the V_1 pulse. The conditioning state was recalled by the subsequent simultaneous application of V_1 and V_4 at pulse numbers of 50 and 70. Note that only a single trial of simultaneous V_1 and V_4 application is enough for the second and third conditioning processes, whereas three trials are required for the first conditioning process. This, however, can be tuned by changing the applied voltage. One set of measurement results is shown in **Figure 7**b with -6.5 V and 6.5 V used for V_1 and V_4, respectively. In this case, conditioning was completed after three simultaneous V_1 and V_4 applications for every conditioning process after initialization. Thus, the required number of times for conditioning is found to be controllable by changing the amplitude of V_1 and V_4. From these experiments, we conclude that the tunable Pavlovian conditioning scheme can successfully be implemented in four-terminal memristive devices.

The oxygen vacancy distribution in the device during the above Pavlovian conditioning process was also examined through electro-coloring phenomena. **Figure 7**c shows typical optical micrographs of the electrically active zone of the device subjected to voltage applications according to the protocol shown in **Figure 7**a. At the initial stage (pulse

number: 0) just after initialization, dark blue regions were observed, mainly around the tips of T3 and T4. After the first conditioning process (pulse number: 30), a strongly colored region was generated at the tip of T1. A similar contrast change in the colored region was confirmed after the second initialization (pulse number: 40) and conditioning (pulse number: 50), where, once again, dark blue T3 and T4 regions and strongly colored T1 regions were observed, respectively. As described above, since the coloration in TiO_{2-x} stems from the increase in the oxygen vacancy concentration at the site, the observed color change reflects a modulation of the oxygen vacancy distribution. During initialization, the electric field causes the oxygen vacancies around T1 and T2 to drift towards T3 and T4 (Figure 7d). The resulting dilution (condensation) of oxygen vacancies around T1 (T3 and T4) likely leads to low $G_{1\text{-}3}$ (high $G_{4\text{-}3}$). On the other hand, during conditioning, the effectively large electric field directed from T4 to T1, induced by the simultaneous application of negative V_1 and positive V_4, causes oxygen vacancies to drift and densely accumulate around T1, thereby leading to a high $G_{1\text{-}3}$. Thanks to these procedures, the conductance state of $G_{1\text{-}3}$ can be switched between LCS and HCS.

The present results directly indicate that variation of the oxygen vacancy distribution in the device's active region plays a crucial role in changing the electrical conductance between the electrode terminals. This gives rise to a rich variety of synapse-based connectionism, which demonstrates that associative learning was successfully implemented as a hetero-synaptic function in a single four-terminal memristive device. In terms of the device structure, our four-terminal memristor may apparently be similar to dual-gated transistors or prototypic JFET models. However, working principle of our device is based on two-dimensional redistribution of oxygen vacancies and this brings striking versatility of memristive characteristics. In synaptic operations mentioned above, not only electrical interaction between two orthogonal pairs of electrodes, interaction between neighboring electrodes that brings oblique modification of vacancy distribution is exploited as in the case of Pavlov's dog demonstration (Fig. 7). This property variation can be further extended by changing shape, number and configuration of electrodes. Exploration of different device configurations and networking will be subjects of interest in future works.

3. Conclusions

In this work, we fabricated four-terminal memristive devices consisting of epitaxial TiO_{2-x} thin films, and characterized their conductive switching properties. Control of memristive properties through the two-dimensional oxygen vacancy distribution enables a rich diversity of artificial synaptic devices, in particular, hetero-synaptic modulation as a higher-order synaptic function. Behavioral habituation/sensitization and STDP were demonstrated, whose characteristics were successfully tuned by the application of a gate voltage to the device, mimicking the roles of hetero-synaptic input signals or neuromodulators. In addition, gate-tunable Pavlovian conditioning (associative learning) was implemented in a single memristive device without the need for transistors or other circuit elements. These results prove the strong capability and versatile functionality of our four-terminal memristive device in which conductance modulation is based on the modification of the two-dimensional distribution of oxygen vacancies in the TiO_{2-x} thin film. Since the device structure is relatively simple, the four electrode terminals can be scaled down to a submicron size and readily arranged into a multi-terminal (more than four) configuration. This facilitates a further extension of functionalities for an advanced synaptic device.

4. Experimental Section

Fabrication of memristive device

Epitaxial thin films of TiO_{2-x} were prepared on non-doped insulative rutile-TiO_2(001) single-crystal substrates by pulsed laser deposition (PLD) using a Nd:YAG laser (λ=266 nm). During deposition, the substrate temperature was kept at 500°C and the oxygen partial pressure was kept constant. The laser fluence was controlled to obtain a growth rate ranging from 2.5 to 3.0 nm/min. The thickness and resistivity of the TiO_{2-x} epitaxial thin films were varied by changing the deposition time and the oxygen partial pressure. After film deposition, planar devices with four-terminal electrodes were fabricated by sputtering Pt films on the TiO_{2-x} film surface through a metal mask. Each electrode was verified in advance to have an ohmic contact with the TiO_{2-x} film, which typically occurs in

highly-doped semiconductor films.

Electrical measurements

All electrical measurements were performed using a prober station inside a vacuum chamber at a base pressure below 10^{-3} Pa and a Keysight B1500A semiconductor device analyzer. The conductances of the devices were calculated from the currents measured between T1 and T3 at an applied voltage of 1 V to investigate the conductance variation during consecutive voltage applications and 100 mV to examine gate voltage effects on the synaptic plasticity of the device.

Simulation model

We performed a two-dimensional (2D) finite element simulation considering the drift and diffusion of *n*-type dopants (oxygen vacancies), and evaluated the dopant density distribution between terminals. First, the carrier density distributions, n and p, and potential distribution, φ, were determined by solving the carrier continuity equations (2) and (3) and the Poisson equation (4). Then, we solved the continuity equation (5) in consideration of the drift and diffusion of dopants to obtain a new donor density distribution, N_{d}.

$$\nabla \cdot \left(qp\mu_{\mathrm{p}}\nabla\varphi + qD_{\mathrm{p}}\nabla p\right) = 0 \tag{2}$$

$$\nabla \cdot (qn\mu_{\mathrm{n}}\nabla\varphi - qD_{\mathrm{n}}\nabla n) = 0 \tag{3}$$

$$\nabla^2\ \varphi = -\frac{q}{\epsilon}(p - n + N_{\mathrm{d}} - N_{\mathrm{a}}) \tag{4}$$

$$q\frac{dN_{\mathrm{d}}}{dt} = \nabla(qN_{\mathrm{d}}\mu_{\mathrm{i}}\nabla\varphi - qD_{\mathrm{i}}\nabla N_{\mathrm{d}}) \tag{5}$$

The modulation of the donor density distribution was evaluated under specific voltage application conditions by solving Eqs. (2), (3), (4), and (5) recursively. For the present simulation, the following parameters were used.

Parameter		Value	Units
permittivity of vacuum	ε_0	8.854×10^{-12}	F/m
elementary charge	e	1.602×10^{-19}	C

Boltzmann constant	k_B	1.381×10^{-23}	J/K
temperature	T	300.0	K
thermal voltage	$v_0 = k_B T/e$	2.552×10^{-2}	V
bandgap energy	E_g	3.000	eV
relative permittivity	ε_r	10.00	-
electron mobility	μ_e	1.0×10^{-4}	$\mathrm{m^2/Vs}$
hole mobility	μ_h	1.0×10^{-4}	$\mathrm{m^2/Vs}$
conduction band density of states	N_c	2.8×10^{25}	$/\mathrm{m^3}$
valence band density of states	N_V	2.8×10^{25}	$/\mathrm{m^3}$
donor density in electrode	N_{d0}	5.0×10^{26}	$/\mathrm{m^3}$
initial donor density of memristor	N_d^*	5.0×10^{25}	$/\mathrm{m^3}$
acceptor density	N_a	5.0×10^{24}	$/\mathrm{m^3}$

Supporting Information

The Supporting Information is available free of charge at https://pubs.acs.org/doi/xxxx.

Additional experimental details and supporting figures; RHEED pattern of the epitaxially grown TiO_{2-x} film; dependence of resistive switching properties on TiO_{2-x} layer resistivity and thickness; endurance and retention properties of conductance states; supplementary figures for gate effects on the STDP property (PDF)

Acknowledgments

This research was supported in part by a KAKENHI Grant-in-Aid (Nos. JP17H03236, JP17K18881, JPK04468, T19K044680, JP20H00248, and JP21K18723) from the Japan Society for the Promotion of Science (JSPS).

Conflict of Interest

The authors declare no conflict of interest.

References

(1) Castellucci, V.; Kandel, E. R. Presynaptic facilitation as a mechanism for behavioral sensitization in Aplysia. *Science* **1976**, *194*, 1176-1178.

(2) Brunelli, M.; Castellucci, V.; Kandel, E. R. Synaptic facilitation and behavioral sensitization in Aplysia: possible role of serotonin and cyclic AMP. *Science* **1976**, *194*, 1178-1181.

(3) Bliss, T. V.; Collingridge, G. L. A synaptic model of memory: long-term potentiation in the hippocampus. *Nature* **1993**, *361*, 31-39.

(4) Stuart, G. J.; Sakmann, B. Active propagation of somatic action potentials into neocortical pyramidal cell dendrites. *Nature* **1994**, *367*, 69-72.

(5) Chua, L. Memristor-the missing circuit element. *IEEE Trans. Circuit Theory* **1971**, *18*, 507-519.

(6) Chua, L. O.; Kang, S. M. Memristive devices and systems. *Proc. IEEE* **1976**, *64*, 209-223.

(7) Strukov, D. B.; Snider, G. S.; Stewart, D. R.; Williams, R. S. The missing memristor found. *Nature* **2008**, *453*, 80-83.

(8) Ohno, T.; Hasegawa, T.; Tsuruoka, T.; Terabe, K.; Gimzewski, J. K.; Aono, M. Short-term plasticity and long-term potentiation mimicked in single inorganic synapses. *Nat. Mater.* **2011**, *10*, 591-595.

(9) Kuzum, D.; Yu, S.; Wong, H. P. Synaptic electronics: materials, devices and applications. *Nanotechnology* **2013**, *24*, 382001.

(10) Ziegler, M.; Soni, R.; Patelczyk, T.; Ignatov, M.; Bartsch, T.; Meuffels, P.; Kohlstedt, H. An electronic version of Pavlov's dog. *Adv. Funct. Mater.* **2012**, *22*, 2744-2749.

(11) Yin, X.-B.; Yang, R.; Xue, K.-H.; Tan, Z.-H.; Zhang, X.-D.; Miao, X.-S.; Guo, X. Mimicking the brain functions of learning, forgetting and explicit/implicit memories with $SrTiO_3$-based memristive devices. *Phys. Chem. Chem. Phys.* **2016**, *18*, 31796-31802.

(12) Jo, S. H.; Chang, T.; Ebong, I.; Bhadviya, B. B.; Mazumder, P.; Lu, W. Nanoscale memristor device as synapse in neuromorphic systems. *Nano Lett.* **2010**, *10*, 1297-1301.

(13) Chanthbouala, A.; Garcia, V.; Cherifi, R. O.; Bouzehouane, K.; Fusil, S.; Moya, X.; Xavier, S.; Yamada, H.; Deranlot, C.; Mathur, N. D. A ferroelectric memristor. *Nat. Mater.* **2012**, *11*, 860-864.

(14) Waser, R.; Dittmann, R.; Staikov, G.; Szot, K. Redox-based resistive switching memories–

nanoionic mechanisms, prospects, and challenges. *Adv. Mater.* **2009**, *21*, 2632-2663.

(15) Yu, S.; Gao, B.; Fang, Z.; Yu, H.; Kang, J.; Wong, H. S. P. A low energy oxide-based electronic synaptic device for neuromorphic visual systems with tolerance to device variation. *Adv. Mater.* **2013**, *25*, 1774-1779.

(16) Seo, K.; Kim, I.; Jung, S.; Jo, M.; Park, S.; Park, J.; Shin, J.; Biju, K. P.; Kong, J.; Lee, K. Analog memory and spike-timing-dependent plasticity characteristics of a nanoscale titanium oxide bilayer resistive switching device. *Nanotechnology* **2011**, *22*, 254023.

(17) Szot, K.; Rogala, M.; Speier, W.; Klusek, Z.; Besmehn, A.; Waser, R. TiO2—a prototypical memristive material. Nanotechnology **2011**, *22*, 254001.

(18) Prezioso, M.; Merrikh-Bayat, F.; Hoskins, B.; Adam, G. C.; Likharev, K. K.; Strukov, D. B. Training and operation of an integrated neuromorphic network based on metal-oxide memristors. Nature **2015**, *521*, 61-64.

(19) Yamaguchi, K.; Takeuchi, S.; Tohei, T.; Ikarashi, N.; Sakai, A. Analysis of Ti valence states in resistive switching regions of a rutile TiO_{2-x} four-terminal memristive device. Jpn. J. Appl. Phys. **2018**, *57*, 06KB02.

(20) Takeuchi, S.; Shimizu, T.; Isaka, T.; Tohei, T.; Ikarashi, N.; Sakai, A. Demonstrative operation of four-terminal memristive devices fabricated on reduced TiO_2 single crystals. *Sci. Rep.* **2019**, *9*, 2601.

(21) Nagata, Z.; Shimizu, T.; Isaka, T.; Tohei, T.; Ikarashi, N.; Sakai, A. Gate tuning of synaptic functions based on oxygen vacancy distribution control in four-terminal TiO_{2-x} memristive devices. *Sci. Rep.* **2019**, *9*, 10013.

(22) Hawkins, R. D.; Abrams, T. W.; Carew, T. J.; Kandel, E. R. A cellular mechanism of classical conditioning in Aplysia: activity-dependent amplification of presynaptic facilitation. *Science* **1983**, *219*, 400-405.

(23) Antonov, I.; Antonova, I.; Kandel, E. R.; Hawkins, R. D. Activity-dependent presynaptic facilitation and Hebbian LTP are both required and interact during classical conditioning in Aplysia. *Neuron* **2003**, *37*, 135-147.

(24) Letellier, M.; Park, Y. K.; Chater, T. E.; Chipman, P. H.; Gautam, S. G.; Oshima-Takago, T.; Goda, Y. Astrocytes regulate heterogeneity of presynaptic strengths in hippocampal networks. *Proc. Natl. Acad. Sci.* **2016**, *113*, E2685-E2694.

(25) De Pittà, M.; Brunel, N.; Volterra, A. Astrocytes: orchestrating synaptic plasticity?

Neuroscience **2016**, *323*, 43-61.

(26) Glanzman, D. L. The cellular basis of classical conditioning in Aplysia californica—it's less simple than you think. *Trends Neurosci.* **1995**, *18*, 30-36.

(27) Bailey, C. H.; Giustetto, M.; Huang, Y.-Y.; Hawkins, R. D.; Kandel, E. R. Is heterosynaptic modulation essential for stabilizing hebbian plasiticity and memory. *Nat. Rev. Neurosci.* **2000**, *1*, 11-20.

(28) Yang, X.; Fang, Y.; Yu, Z.; Wang, Z.; Zhang, T.; Yin, M.; Lin, M.; Yang, Y.; Cai, Y.; Huang, R. Nonassociative learning implementation by a single memristor-based multi-terminal synaptic device. *Nanoscale* **2016**, *8*, 18897-18904.

(29) Xia, Q.; Pickett, M. D.; Yang, J. J.; Li, X.; Wu, W.; Medeiros-Ribeiro, G.; Williams, R. S. Two-and three-terminal resistive switches: nanometer-scale Memristors and Memistors. *Adv. Funct. Mater.* **2011**, *21*, 2660-2665.

(30) Li, Y.; Xu, L.; Zhong, Y. P.; Zhou, Y. X.; Zhong, S. J.; Hu, Y. Z.; Chua, L. O.; Miao, X. S. Associative Learning with Temporal Contiguity in a Memristive Circuit for Large-Scale Neuromorphic Networks. *Adv. Electro. Mater.* **2015**, *1*, 1500125.

(31) Tan, Z.-H.; Yin, X.-B.; Yang, R.; Mi, S.-B.; Jia, C.-L.; Guo, X. Pavlovian conditioning demonstrated with neuromorphic memristive devices. *Sci. Rep.* **2017**, *7*, 1-10.

(32) Yang, L.; Zeng, Z.; Wen, S. A full-function Pavlov associative memory implementation with memristance changing circuit. *Neurocomputing* **2018**, *272*, 513-519.

(33) Shi, J.; Ha, S. D.; Zhou, Y.; Schoofs, F.; Ramanathan, S. A correlated nickelate synaptic transistor. *Nat. Commun.* **2013**, *4*, 2676.

(34) Sacchetto, D.; Gaillardon, P.-E.; Zervas, M.; Carrara, S.; De Micheli, G.; Leblebici, Y. Applications of multi-terminal memristive devices: a review. *IEEE Circuits and Systems Magazine* **2013**, *13*, 23-41.

(35) Zhu, L. Q.; Wan, C. J.; Guo, L. Q.; Shi, Y.; Wan, Q. Artificial synapse network on inorganic proton conductor for neuromorphic systems. *Nat. Commun.* **2014**, *5*, 3158.

(36) Yang, Y.; Chen, B.; Lu, W. D. Memristive physically evolving networks enabling the emulation of heterosynaptic plasticity. *Adv. Mater.* **2015**, *27*, 7720-7727.

(37) Sangwan, V. K.; Jariwala, D.; Kim, I. S.; Chen, K.-S.; Marks, T. J.; Lauhon, L. J.; Hersam, M. C. Gate-tunable memristive phenomena mediated by grain boundaries in single-layer MoS_2. *Nat. Nanotechnol.* **2015**, *10*, 403-406.

(38) Sangwan, V. K.; Lee, H.-S.; Bergeron, H.; Balla, I.; Beck, M. E.; Chen, K.-S.; Hersam, M. C. Multi-terminal memtransistors from polycrystalline monolayer molybdenum disulfide. *Nature* **2018**, *554*, 500-504.

(39) Sangwan, V. K.; Hersam, M. C. Neuromorphic nanoelectronic materials. *Nat. Nanotechnol.* **2020**, *15*, 517-528.

(40) Maier, P.; Hartmann, F.; Emmerling, M.; Schneider, C.; Kamp, M.; Worschech, L.; Höfling, S. Associative learning with Y-shaped floating gate transistors operated in memristive modes. *Appl. Phys. Lett.* **2017**, *110*, 053503.

(41) Yang, Y.; Yin, M.; Yu, Z.; Wang, Z.; Zhang, T.; Cai, Y.; Lu, W. D.; Huang, R. Multifunctional Nanoionic Devices Enabling Simultaneous Heterosynaptic Plasticity and Efficient In-Memory Boolean Logic. *Adv. Electron. Mater.* **2017**, *3*, 1700032.

(42) Zhu, X.; Li, D.; Liang, X.; Lu, W. D. Ionic modulation and ionic coupling effects in MoS_2 devices for neuromorphic computing. *Nat. Mater.* **2019**, *18*, 141-148.

(43) Guo, J.; Wang, L.; Liu, Y.; Zhao, Z.; Zhu, E.; Lin, Z.; Wang, P.; Jia, C.; Yang, S.; Lee, S.-J. Highly reliable low-voltage memristive switching and artificial synapse enabled by van der Waals integration. *Matter* **2020**, *2*, 965-976.

(44) He, C.; Tang, J.; Shang, D.-S.; Tang, J.; Xi, Y.; Wang, S.; Li, N.; Zhang, Q.; Lu, J.-K.; Wei, Z. Artificial synapse based on van der Waals heterostructures with tunable synaptic functions for neuromorphic computing. *ACS Appl. Mater. Interfaces* **2020**, *12*, 11945-11954.

(45) Long, T. Y.; Zhu, L. Q.; Ren, Z. Y.; Guo, Y. B. Global modulatory heterosynaptic mechanisms in bio-polymer electrolyte gated oxide neuron transistors. *J. Phys. D: Appl. Phys.* **2020**, *53*, 435105.

(46) He, H.-K.; Yang, R.; Huang, H.-M.; Yang, F.-F.; Wu, Y.-Z.; Shaibo, J.; Guo, X. Multi-gate memristive synapses realized with the lateral heterostructure of 2D WSe_2 and WO_3. *Nanoscale* **2020**, *12*, 380-387.

(47) Cheng, Y.; Li, H.; Liu, B.; Jiang, L.; Liu, M.; Huang, H.; Yang, J.; He, J.; Jiang, J. Vertical 0D-Perovskite/2D-MoS_2 van der Waals Heterojunction Phototransistor for Emulating Photoelectric-Synergistically Classical Pavlovian Conditioning and Neural Coding Dynamics. *Small* **2020**, *16*, 2005217.

(48) Lee, G.; Baek, J. H.; Ren, F.; Pearton, S. J.; Lee, G. H.; Kim, J. Artificial Neuron and

Synapse Devices Based on 2D Materials. *Small* **2021**, *17*, 2100640.

(49) Ding, G.; Yang, B.; Chen, R. S.; Mo, W. A.; Zhou, K.; Liu, Y.; Shang, G.; Zhai, Y.; Han, S. T.; Zhou, Y. Reconfigurable 2D WSe_2-Based Memtransistor for Mimicking Homosynaptic and Heterosynaptic Plasticity. *Small* **2021**, *17*, 2103175.

(50) Miyaoka, H.; Mizutani, G.; Sano, H.; Omote, M.; Nakatsuji, K.; Komori, F. Anomalous electro-migration of oxygen vacancies in reduced TiO_2. *Solid State Commun.* **2002**, *123*, 399-404.

(51) Moballegh, A.; Dickey, E. C. Electric-field-induced point defect redistribution in single-crystal TiO_{2-x} and effects on electrical transport. *Acta Mater.* **2015**, *86*, 352-360.

(52) Strukov, D. B.; Borghetti, J. L.; Williams, R. S. Coupled ionic and electronic transport model of thin-film semiconductor memristive behavior. *Small* **2009**, *5*, 1058-1063.

(53) Aoki, Y.; Wiemann, C.; Feyer, V.; Kim, H.-S.; Schneider, C. M.; Ill-Yoo, H.; Martin, M. Bulk mixed ion electron conduction in amorphous gallium oxide causes memristive behaviour. *Nat. Commun.* **2014**, *5*, 3473.

(54) Marchewka, A.; Roesgen, B.; Skaja, K.; Du, H.; Jia, C. L.; Mayer, J.; Rana, V.; Waser, R.; Menzel, S. Nanoionic resistive switching memories: On the physical nature of the dynamic reset process. *Adv. Electron. Mater.* **2016**, *2*, 1500233.

(55) Markram, H.; Lübke, J.; Frotscher, M.; Sakmann, B. Regulation of synaptic efficacy by coincidence of postsynaptic APs and EPSPs. *Science* **1997**, *275*, 213-215.

(56) Bi, G.; Poo, M. Synaptic modifications in cultured hippocampal neurons: dependence on spike timing, synaptic strength, and postsynaptic cell type. *J. Neurosci.* **1998**, *18*, 10464-10472.

(57) Shulz, D.; Feldman, D. Spike timing-dependent plasticity. *Rubenstein JLR, Rakic P. Comprehensive developmental neuroscience: neural circuit development and function in the healthy and diseased brain. San Diego, CA: Elsevier* **2013**, Ch.9.

(58) Fino, E.; Glowinski, J.; Venance, L. Bidirectional activity-dependent plasticity at corticostriatal synapses. *J. Neurosci.* **2005**, *25*, 11279-11287.

(59) Lamsa, K. P.; Heeroma, J. H.; Somogyi, P.; Rusakov, D. A.; Kullmann, D. M. Anti-Hebbian long-term potentiation in the hippocampal feedback inhibitory circuit. *Science* **2007**, *315*, 1262-1266.

(60) Fino, E.; Deniau, J. M.; Venance, L. Cell-specific spike-timing-dependent plasticity in

GABAergic and cholinergic interneurons in corticostriatal rat brain slices. *J. Physiol.* **2008**, *586*, 265-282.

(61) Koch, G.; Ponzo, V.; Di Lorenzo, F.; Caltagirone, C.; Veniero, D. Hebbian and anti-Hebbian spike-timing-dependent plasticity of human cortico-cortical connections. *J. Neurosci.* **2013**, *33*, 9725-9733.

(62) Lai, Q.; Zhang, L.; Li, Z.; Stickle, W. F.; Williams, R. S.; Chen, Y. Ionic/electronic hybrid materials integrated in a synaptic transistor with signal processing and learning functions. *Adv. Mater.* **2010**, *22*, 2448-2453.

(63) Kuzum, D.; Jeyasingh, R. G.; Lee, B.; Wong, H.-S. P. Nanoelectronic programmable synapses based on phase change materials for brain-inspired computing. *Nano Lett.* **2012**, *12*, 2179-2186.

(64) Krzysteczko, P.; Münchenberger, J.; Schäfers, M.; Reiss, G.; Thomas, A. The Memristive Magnetic Tunnel Junction as a Nanoscopic Synapse-Neuron System. *Adv. Mater.* **2012**, *24*, 762-766.

(65) Li, Y.; Zhong, Y.; Zhang, J.; Xu, L.; Wang, Q.; Sun, H.; Tong, H.; Cheng, X.; Miao, X. Activity-dependent synaptic plasticity of a chalcogenide electronic synapse for neuromorphic systems. *Sci. Rep.* **2014**, *4*, 4906.

(66) Nikiruy, K.; Emelyanov, A.; Demin, V.; Sitnikov, A.; Minnekhanov, A.; Rylkov, V.; Kashkarov, P.; Kovalchuk, M. Dopamine-like STDP modulation in nanocomposite memristors. *AIP Advances* **2019**, *9*, 065116.

(67) Reynolds, J. N.; Wickens, J. R. Dopamine-dependent plasticity of corticostriatal synapses. *Neural Networks* **2002**, *15*, 507-521.

(68) Bissière, S.; Humeau, Y.; Lüthi, A. Dopamine gates LTP induction in lateral amygdala by suppressing feedforward inhibition. *Nat. Neurosci.* **2003**, *6*, 587-592.

(69) Seol, G. H.; Ziburkus, J.; Huang, S.; Song, L.; Kim, I. T.; Takamiya, K.; Huganir, R. L.; Lee, H.-K.; Kirkwood, A. Neuromodulators control the polarity of spike-timing-dependent synaptic plasticity. *Neuron* **2007**, *55*, 919-929.

(70) Couey, J. J.; Meredith, R. M.; Spijker, S.; Poorthuis, R. B.; Smit, A. B.; Brussaard, A. B.; Mansvelder, H. D. Distributed network actions by nicotine increase the threshold for spike-timing-dependent plasticity in prefrontal cortex. *Neuron* **2007**, *54*, 73-87.

(71) Zhang, J.-C.; Lau, P.-M.; Bi, G.-Q. Gain in sensitivity and loss in temporal contrast of

STDP by dopaminergic modulation at hippocampal synapses. *Proc. Natl. Acad. Sci.* **2009**, *106*, 13028-13033.

(72) Pawlak, V.; Wickens, J. R.; Kirkwood, A.; Kerr, J. N. Timing is not everything: neuromodulation opens the STDP gate. *Front. Synaptic Neurosci.* **2010**, *2*, 146.

(73) Ruan, H.; Saur, T.; Yao, W.-D. Dopamine-enabled anti-Hebbian timing-dependent plasticity in prefrontal circuitry. *Front. Neural Circuits* **2014**, *8*, 38.

(74) Yang, K.; Dani, J. A. Dopamine D1 and D5 receptors modulate spike timing-dependent plasticity at medial perforant path to dentate granule cell synapses. *J. Neurosci.* **2014**, *34*, 15888-15897.

(75) Foncelle, A.; Mendes, A.; Jędrzejewska-Szmek, J.; Valtcheva, S.; Berry, H.; Blackwell, K. T.; Venance, L. Modulation of spike-timing dependent plasticity: towards the inclusion of a third factor in computational models. *Front. Comput. Neurosci.* **2018**, *12*, 49.

(76) Shen, W.; Flajolet, M.; Greengard, P.; Surmeier, D. J. Dichotomous dopaminergic control of striatal synaptic plasticity. *Science* **2008**, *321*, 848-851.

(77) Cassenaer, S.; Laurent, G. Conditional modulation of spike-timing-dependent plasticity for olfactory learning. *Nature* **2012**, *482*, 47-52.

(78) Kuśmierz, Ł.; Isomura, T.; Toyoizumi, T. Learning with three factors: modulating Hebbian plasticity with errors. *Current Opinion in Neurobiology* **2017**, *46*, 170-177.

(79) Sabec, M. H.; Wonnacott, S.; Warburton, E. C.; Bashir, Z. I. Nicotinic acetylcholine receptors control encoding and retrieval of associative recognition memory through plasticity in the medial prefrontal cortex. *Cell Rep.* **2018**, *22*, 3409-3415.

(80) Frémaux, N.; Gerstner, W. Neuromodulated spike-timing-dependent plasticity, and theory of three-factor learning rules. *Front. Neural Circuits* **2016**, *9*, 85.

(81) Brzosko, Z.; Mierau, S. B.; Paulsen, O. Neuromodulation of spike-timing-dependent plasticity: past, present, and future. *Neuron* **2019**, *103*, 563-581.

(82) Malenka, R. C.; Nicoll, R. A. Silent synapses speak up. *Neuron* **1997**, *19*, 473-476.

(83) Kerchner, G. A.; Nicoll, R. A. Silent synapses and the emergence of a postsynaptic mechanism for LTP. *Nat. Rev. Neurosci.* **2008**, *9*, 813-825.

(84) Arendt, K. L.; Sarti, F.; Chen, L. Chronic inactivation of a neural circuit enhances LTP by inducing silent synapse formation. *J. Neurosci.* **2013**, *33*, 2087-2096.

(85) Vincent-Lamarre, P.; Lynn, M.; Béïque, J.-C. The eloquent silent synapse. *Trends*

Neurosci. **2018**, *41*, 557-559.

(86) Barbosa, J.; Stein, H.; Martinez, R. L.; Galan-Gadea, A.; Li, S.; Dalmau, J.; Adam, K. C.; Valls-Solé, J.; Constantinidis, C.; Compte, A. Interplay between persistent activity and activity-silent dynamics in the prefrontal cortex underlies serial biases in working memory. *Nat. Neurosci.* **2020**, *23*, 1016-1024.

(87) Xu, W.; Löwel, S.; Schlüter, O. M. Silent synapse-based mechanisms of critical period plasticity. *Front. Cell. Neurosci.* **2020**, *14*, 213.

(88) Srivastava, N.; Hinton, G.; Krizhevsky, A.; Sutskever, I.; Salakhutdinov, R. Dropout: a simple way to prevent neural networks from overfitting. *J. Machine Learning Research* **2014**, *15*, 1929-1958.

(89) Pinsker, H.; Kupfermann, I.; Castellucci, V.; Kandel, E. Habituation and dishabituation of the GM-withdrawal reflex in Aplysia. *Science* **1970**, *167*, 1740-1742.

(90) Kupfermann, I.; Castellucci, V.; Pinsker, H.; Kandel, E. Neuronal correlates of habituation and dishabituation of the gill-withdrawal reflex in Aplysia. *Science* **1970**, *167*, 1743-1745.

(91) Castellucci, V.; Pinsker, H.; Kupfermann, I.; Kandel, E. R. Neuronal mechanisms of habituation and dishabituation of the gill-withdrawal reflex in Aplysia. *Science* **1970**, *167*, 1745-1748.

(92) Hawkins, R.; Castellucci, V.; Kandel, E. Interneurons involved in mediation and modulation of gill-withdrawal reflex in Aplysia. II. Identified neurons produce heterosynaptic facilitation contributing to behavioral sensitization. *J. Neurophysiol.* **1981**, *45*, 315-328.

(93) Frost, L.; Kaplan, S. W.; Cohen, T. E.; Henzi, V.; Kandel, E. R.; Hawkins, R. D. A simplified preparation for relating cellular events to behavior: contribution of LE and unidentified siphon sensory neurons to mediation and habituation of the Aplysia gill-and siphon-withdrawal reflex. *J. Neurosci.* **1997**, *17*, 2900-2913.

(94) Antonov, I.; Kandel, E. R.; Hawkins, R. D. The contribution of facilitation of monosynaptic PSPs to dishabituation and sensitization of the Aplysia siphon withdrawal reflex. *J. Neurosci.* **1999**, *19*, 10438-10450.

(95) Carew, T. J.; Castellucci, V. F.; Kandel, E. R. An analysis of dishabituation and sensitization of the gill-withdrawal reflex in Aplysia. *Int. J. Neurosci.* **1971**, *2*, 79-98.

(96) Pinsker, H. M.; Hening, W. A.; Carew, T. J.; Kandel, E. R. Long-term sensitization of a

defensive withdrawal reflex in Aplysia. *Science* **1973**, *182*, 1039-1042.

(97) Pavlov, I. P. Experimental Psychology and Psychopathology in Animals1. In *Psychopathology and Psychiatry*, *Taylor & Francis Group*, *New York*, **1994**, Ch.2.

Table 1. Truth table for Pavlovian conditioning before and after learning.

bell sound	food	response (before conditioning)	response (after conditioning)
0	0	0	0
0	1	1	1
1	1	1	1
1	0	0	1

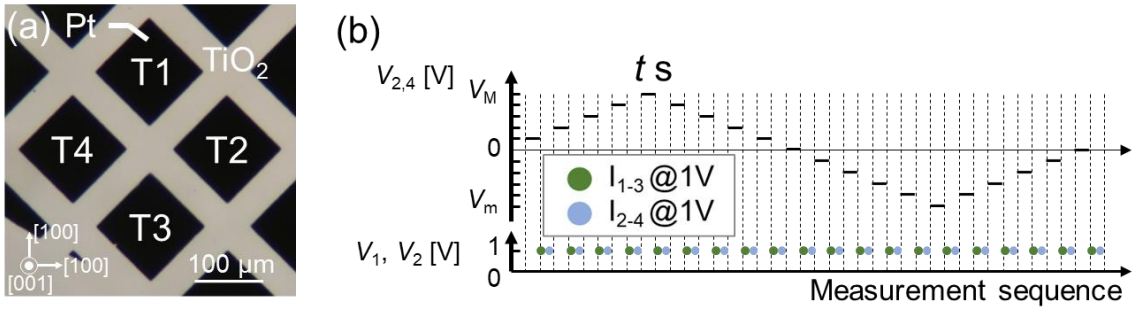

Figure 1

(a) Optical micrograph of a four-terminal planar memristive device fabricated on a TiO_{2-x} epitaxial thin film. (b) Time series of applied write voltage $V_{2,4}$ and read voltages V_1 and V_2. $I_{1\text{-}3}$ and $I_{2\text{-}4}$ were measured at 1 V between consecutive steps of $V_{2,4}$ application.

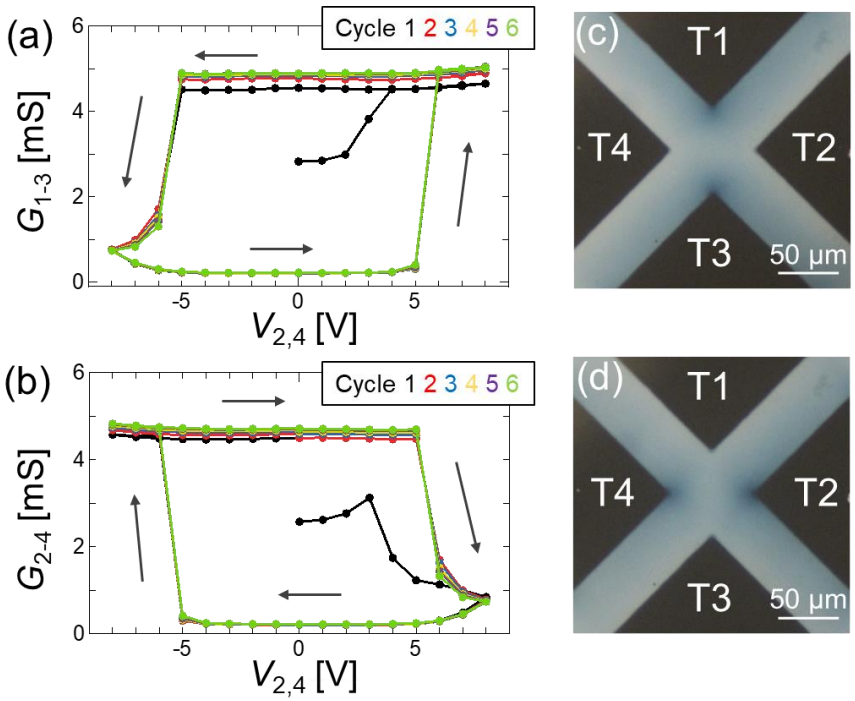

Figure 2

Variation of (a) $G_{1\text{-}3}$ and (b) $G_{2\text{-}4}$ with $V_{2,4}$. (c), (d) Optical micrographs showing internal structure of device just after application of (c) $V_{2,4}$ = 8 V and (d) $V_{2,4}$ = -8 V in cycle 2.

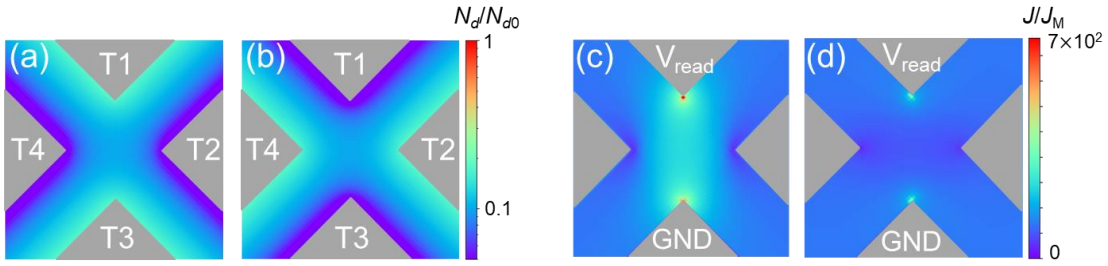

Figure 3

Simulation results for (a), (b) oxygen vacancy concentration (OVC) distribution and (c), (d) current density (CD) distribution, obtained at (a), (c) V_M and (b), (d) V_m. The calculated OVC and CD values were normalized by the N_{d0} (donor density in electrode) and the J_M (maximum current density), respectively.

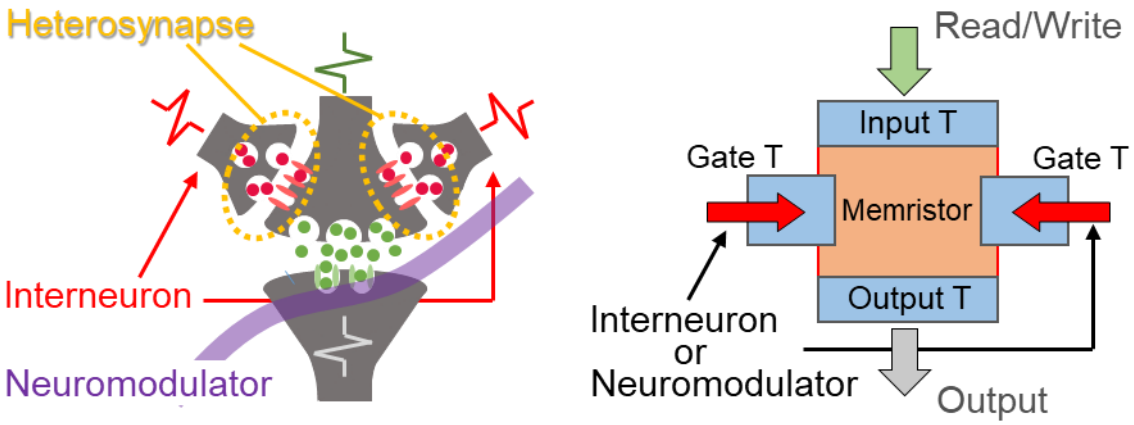

Figure 4

Schematics comparing a biological heterosynapse and neuromodulator (left) and a four-terminal memristive device (right).

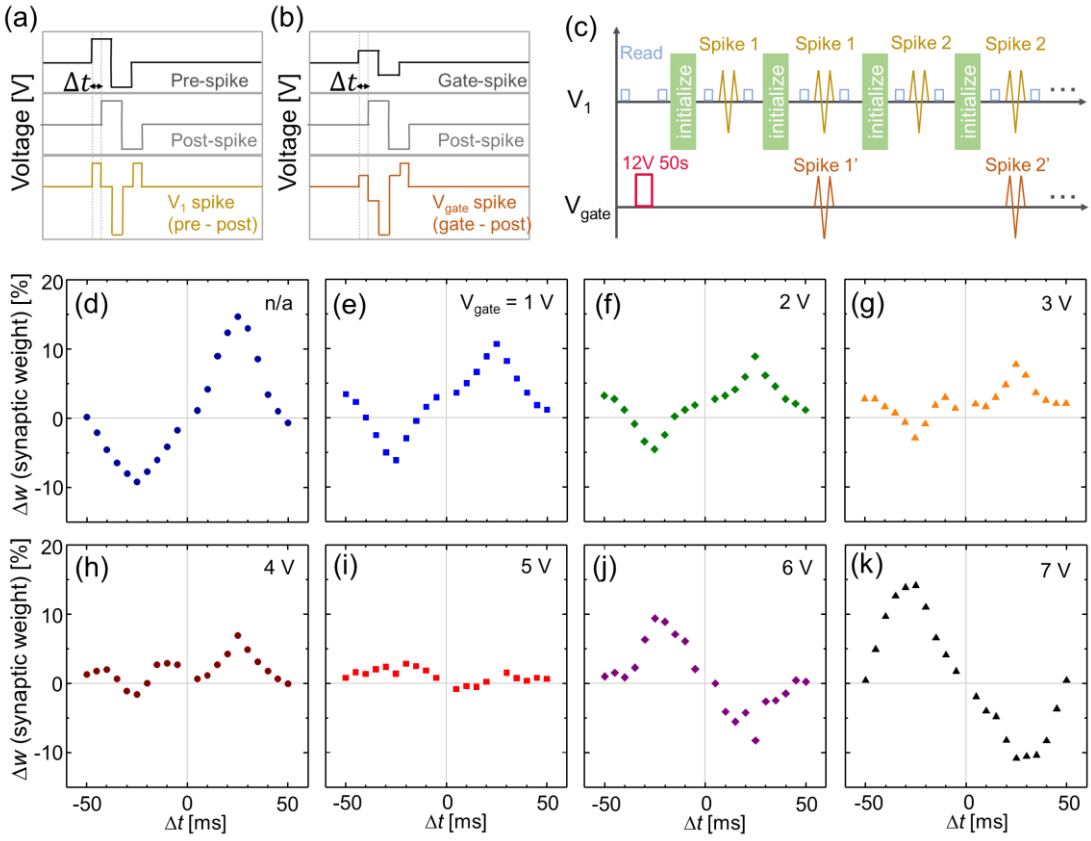

Figure 5

(a), (b) Designed spike pulse schemes used to impart STDP properties. The upper, middle, and lower parts in (a) show pre-spike, post-spike, and total effective voltage applied to T1, respectively. The upper, middle, and lower parts in (b) show gate-spike, post-spike, and effective voltage applied to T2 and T4. (c) Time series of applied voltage V_1 and V_{gate}. $I_{1\text{-}3}$ and $I_{2\text{-}4}$ were measured at 100 mV. (d)-(k) Experimental STDP results. The synaptic weight change Δw is plotted as a function of the time difference Δt for each V_{gate}.

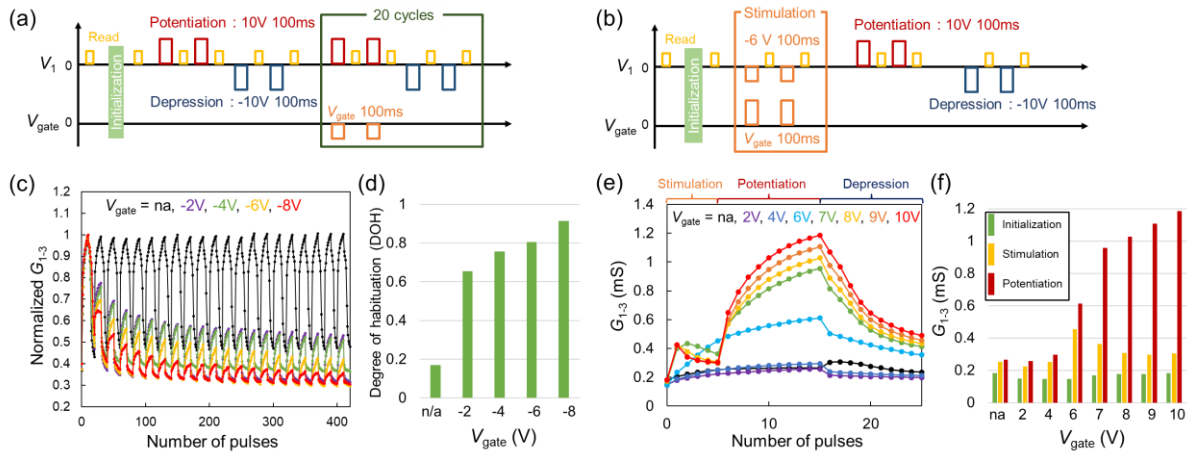

Figure 6

Voltage application protocol for (a) habituation and (b) sensitization. V_1 is applied to T1 for the P/D operation and V_{HG} is applied to both T2 and T4 simultaneously with V_1 in the habituation. The stimulation process with V_{gate} is employed prior to the P/D operation in the sensitization. (c) Modulation of $G_{1\text{-}3}$ with V_{HG} = n/a, -2, -4, -6, and -8 V, showing the habituation characteristics. (d) Degree of habituation (DOH) as a function of V_{HG}. DOH was derived from an equation; DOH=1−($\Delta G_{1\text{-}3,LP}$)/ ($\Delta G_{1\text{-}3,IP}$) where $\Delta G_{1\text{-}3,LP}$ ($\Delta G_{1\text{-}3,IP}$) is the conductance change at the last (initial) potentiation process. (e) Modulation of $G_{1\text{-}3}$ with V_{SG} = n/a, 2, 4, 6, 7, 8, 9, and 10 V, showing the sensitization characteristics. (f) V_{SG} dependence of $G_{1\text{-}3}$ of the initial state, after the stimulation, and after the potentiation.

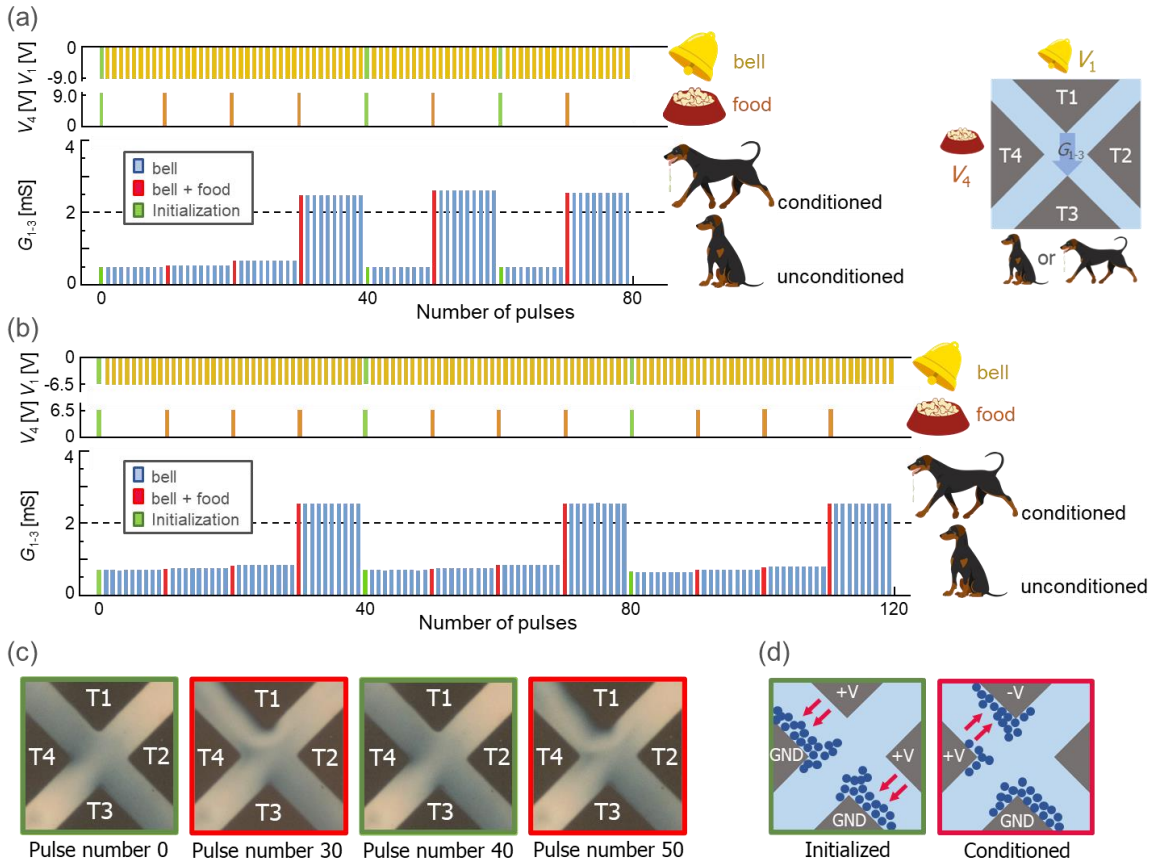

Figure 7

Voltage application protocol emulating Pavlovian conditioning and resultant conductance $G_{1\text{-}3}$ change with voltage amplitudes of (a) V_1 = -9 V, V_4 = 9 V and (b) V_1 = -6.5 V, V_4 = 6.5 V. Inset of (a) illustrates correspondence between four-terminal memristive device and Pavlovian conditioning; V_1 corresponding to the bell sound (upper), V_4 to the food (middle), and $G_{1\text{-}3}$ to the dog's response (lower). (c) Optical micrographs taken after voltage application, corresponding to 0, 30, 40, and 50 pulses in (a). (d) Schematics depicting oxygen vacancy distribution for initialized and conditioned states.

Table of Contents (TOC)/Abstract Graphic